Modelling ion propulsion plume interactions with spacecraft in formation flight

R. Kafafy
International Islamic University Malaysia
Kuala Lumpur
Malaysia

Y. Cao
Harbin Institute of Technology, Shenzhen Graduate School
Shenzhen
China

ABSTRACT

This paper presents a simulation study of ion thruster plume effects on formation flying spacecraft. Two formation flight applications using micro-ion propulsion are considered: an L2-Halo orbit interferometer formation and a LEO micro-satellite formation. Worst case scenarios in both missions have been investigated. We focus our study on thruster configurations resulting in possible indirect plume impingement on satellites outside of the direct impingement zone. Indirect impingement which cannot be predicted except through plasma simulation or in-flight measurements might expose critical spacecraft elements such as optical sensors to a harsh contamination environment. A high-fidelity electrostatic plasma simulation code for parallel computing platforms was used in the study.

In our study, we found that using miniature scale ion propulsion in both formation missions creates a very low charge-exchange plasma environment which results in tolerable contamination environment for other spacecraft in the formation.

NOMENCLATURE

a	correction factor in the analytical beam function
A_e	thruster exit area
E	electrostatic field vector
e	electron charge
F	electrostatic force vector
j_b	beam ion current density
J_{ac}	acceleration grid impingement current
k	Boltzmann constant
k_1, k_2	constants of charge-exchange collision cross section
M	atomic mass (kg)
n	number density
n_e	electron number density
n_{eo}	reference plasma electron number density
n_{bc}	average beam ion number density at center of thruster exit
n_{nc}	average neutral efflux number density at center of thruster exit
n_1	reference plasma number density
n_i	ion number density
R	distance from the point of interest to the beam source point
r	normal distance to the beam centerline
r_T	thruster exit radius
T_e	electron temperature
T_{e0}	reference plasma electron temperature
v	ion velocity vector
v_b	average beam ion velocity
v_{ti}	ion thermal velocity
X	ion position vector
Y	sputtering yield (specifically for molybdenum when bombarded by xenon ions)
dn_{cex}/dt	average production rate of charge exchange ions
dn_{cex_c}/dt	average production rate of charge exchange ions at thruster exit center

Paper No. 3488. Manuscript received 6 August 2009, revised version received 23 October 2009, 2nd revised version received 12 January 2010, accepted 21 January 2010.

https://doi.org/10.1017/S0001924000003894 Published online by Cambridge University Press

Subscripts

b	beam
c	thruster exit center point
cex	charge-exchange collision
n	neutral efflux
0	reference plasma

Greek

α	angular position of the edge of thruster exit measured from the beam centerline
γ, λ	constants of the analytical beam function
ε	electric permittivity
ϕ	electrostatic potential
ϕ_0	reference plasma electrostatic potential
ϕ_{sc}	spacecraft ground potential
$d\Gamma/dt$	Mo^+ flux rate($m^{-2}s^{-1}$)
θ	angular position of the point of interest measured from the beam centerline
ρ	molybdenum density (kg/m^3)
σ	collision cross section
$d\xi/dt$	deposition rate [Å/khr] of molybdenum
$d\eta/dt$	sputtering rate of molybdenum

1.0 INTRODUCTION

Formation flight is being considered for several Earth-orbiting and interplanetary missions. One of the greatest challenges to formation flying is to maintain the formation in orbit within a predetermined tolerance against orbital disturbances such as atmospheric drag, J2-perturbations, etc[1]. Orbital corrections for perturbations are typically small yet frequent, which requires the utilisation of a propulsion system with high specific impulse and low impulse bit. Electric propulsion, in particular ion propulsion, has emerged as one of the best propulsion options for orbit maintenance for spacecraft in formation flying. In fact, various electric propulsion concepts have been proposed.

One of the major concerns in formation flying is the adverse effect caused by the thruster exhaust plume as the existence of other satellites in close proximity may expose critical surfaces to direct or indirect plume impingement. Placing satellites outside of the thruster exhaust zone from neighbouring satellites eliminates direct plume impingement. While such an approach is sufficient to mitigate plume effects for satellites using chemical thrusters, it may not be sufficient for satellites using ion thrusters. The ion thruster exhaust plume is composed of propellant efflux (high energy beam ions, neutralising electrons, and un-ionised neutrals), nonpropellant effluent (materials sputtered from thruster components), and a low energy charge exchange plasma generated by collisions between the beam ions and neutrals within the plume. It is well known that both the low energy charge-exchange (CEX) ions and the ionised sputtered particles can be pushed out of the plume by the local electric field and backflow to interact with the spacecraft. Hence, when using ion propulsion, a satellite outside of the direct plume impingement zone can still be affected by the plume.

This paper presents a modelling study to understand plume effects from indirect plume impingement on formation flying satellites using ion propulsion. Ion thruster plume effects is a subject of intensive modelling and experimental studies as well as one of the main in-flight investigations aboard NASA's Deep Space 1 spacecraft, the first interplanetary spacecraft using ion propulsion[2-11]. However, all these previous studies are concerned with a single spacecraft and the objective was to investigate plume effects on the thruster's host spacecraft. This paper considers a cluster of satellites and the objective is to investigate plume effects on neighboring satellites.

We study plume effects for two formation flying applications. The first is a deep space formation flying mission for space interferometery in an L2-Halo orbit. The L2-Halo orbit formation-flying interferometery concept was previously considered for the NASA's TPF project[12], which has been indefinitely deferred and was carefully studied for the ESA's Darwin project[13]. Based on the Herschel design, three (or four) spacecraft of the Darwin constellation would have carried 3-4m telescopes or light collectors, which would have redirected light to the central hub spacecraft. To meet its objective to find and investigate Earth-like planets, Darwin would have used a technique called nulling interferometry which allows light from distant planets to be combined constructively, showing the planet. Otherwise, starlight would overwhelm the planets' feeble glow. Lately, NASA and ESA considered collaboration on the Darwin mission[14].

The second application is a Low-Earth Orbit (LEO) formation flying of Earth observation micro-satellites which is inspired by the MR SAT of University of Missouri–Rolla[1]. The MR SAT is comprised of two satellites; a primary satellite of approximately 20kg with dimensions 45 × 45 × 45cm; and a secondary satellite of approximately 5kg with dimensions 30 × 30 × 13cm. On orbit, the two satellites are separated by a 10-m tether. After flying in the tethered formation for a predetermined time period, the tether is released. The following satellite will then attempt to maintain formation with the passive leader satellite using limited onboard thrusting capability. The main objectives of the MR SAT mission are to maintain a close formation between the leader/follower within a 10m radius and control the relative position of the follower within ±1m of the nominal 10m separation.

The simulation model is based on the Particle-in-Cell (PIC) method[15] and is extended from our previous studies on plume interactions with a single spacecraft. To resolve the complex boundary conditions imposed by formation flying satellite and to carry out large scale simulations for a simulation domain containing several satellite, the model is implemented using the immersed-finite-element PIC (IFE-PIC) algorithm on parallel computers[10,16,17]. Our previous study has demonstrated that the parallel IFE-PIC approach can be applied to perform high resolution plume simulation with a high parallel efficiency on super computers[10].

Section 2.0 describes the ion propulsion plume–spacecraft interaction model. Section 3.0 briefly discusses the algorithm and parallel implementation. Section 4.0 presents simulation results. Section 5.0 contains a summary and conclusions.

2.0 SPACECRAFT–PLUME INTERACTIONS MODEL

The ion thruster plume interaction model is adapted from the models of Samanta Roy *et al*[2] and Wang *et al*[7]. The model consists of an ion thruster plume model and a spacecraft model.

2.1 Ion thruster plume model

As no definite ion thruster design has been selected for an actual formation flight mission, we shall assume that the ion thrusters used on the cluster satellites for the two mission examples considered in this paper is similar to that of the Jet Propulsion Lab (JPL) Miniature Xenon Ion thruster (MiXI)[12]. MiXI is down-scaled from the NASA NSTAR (Solar Electric Propulsion Technology Application Readiness) ion thruster. It has a 3cm exit diameter, a thrust level of about 0·5 – 3mN and a specific impulse of about 3,000s[12]. These parameters will be used in the ion thruster model of this paper. We assume that the thruster plume of MiXI consists of the same major components of the NSTAR thruster plume,

- propellant beam ions,
- unionised propellant neutrals,

https://doi.org/10.1017/S0001924000003894 Published online by Cambridge University Press

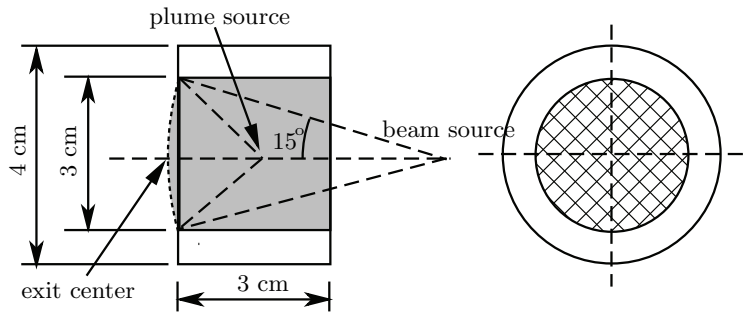


Figure 1. Miniature xenon ion thruster (MiXI) model.

- slow propellant ions created by CEX reaction collisions,
- non-propellant efflux (NPE) which is mainly made of sputtered thruster grid material, and
- neutralising electrons.

Illustration of the ion thruster model is shown in Fig. 1. Similar to Refs 2 and 7, the propellant ion beam profile and the neutral plume density profile are modeled analytically

$$j_{b_c} = \left(\frac{R_c}{R}\right)^2 \left[1-(\frac{\theta}{\alpha})^2\right], \qquad \theta < \gamma\alpha$$
$$j_{b_c} = \exp(\frac{-r}{\lambda})\left(\frac{R_c}{R}\right)^2 \left[1-(\frac{\theta}{\alpha})^2\right], \quad \theta \geq \gamma\alpha \qquad \ldots (1)$$

$$n_n(R,\theta) = a\frac{n_{n_c}}{2}\left(1-\left[1+(\frac{r_T}{R})\right]^{-1/2}\right)\mathrm{Cos}\theta \qquad \ldots (2)$$

where $j_{bc} = ev_b n_{bc}$

Using the analytical profiles for the beam ions and the neutral plume, one could obtain the following spatial distribution of the CEX ion production rate[7].

$$\frac{\mathrm{d}n_{cex}}{\mathrm{d}t} = \sigma_{cex} v_b n_b(\mathbf{x}) n_n(\mathbf{x}) = \frac{n_b(\mathbf{x})}{n_{b_c}} \frac{n_n(\mathbf{x})}{n_{n_c}} \frac{\mathrm{d}n_{cex_c}}{\mathrm{d}t} \qquad \ldots (3)$$

The average CEX ion production rate at the thruster exit is given by;

$$\frac{\mathrm{d}n_{cex_c}}{\mathrm{d}t} = \sigma_{cex} v_b n_{bc} n_{n_c} \qquad \ldots (4)$$

The cross-sections of CEX collisions between monatomic ions, such as Xe+, and their parent gases can be calculated as a function of the ion velocity[18] which may be expressed as;

$$\sigma_{cex} = (k_1 \mathrm{In} v_b + k_2)^2 \qquad \ldots (5)$$

where $k_1 = -0{\cdot}8821 \times 10^{-10}\mathrm{m}^2$ and $k_2 = 15{\cdot}1262 \times 10^{-10}\mathrm{m}^2$ for Xe[2]. The values n_{b_c}, n_{n_c} and $\mathrm{d}n_{cex_0}/\mathrm{d}t$ need to be determined from ion thruster operation conditions. Here, we shall assume that the thruster considered here has the same specific impulse and current density as the NSTAR thruster. Hence, the beam ion density n_{b_c} and the neutral density n_{n_c} at thruster exit have the same value as the NSTAR ion thruster under the Deep Space 1 operating condition. Electrons are assumed isothermal and their density is described by a Boltzmann distribution

$$n_e = n_{e_0} \exp\left[\frac{e(\Phi - \Phi_0)}{kT_{e_0}}\right] \qquad \ldots (6)$$

We assume that the electron temperature T_{e_o} and the plume potential with respect to spacecraft $\Phi_0 - \Phi_{sc}$ are the same as those observed from Deep Space 1 in-flight measurements[5,7].

The sputtered molybdenum (Mo) atoms from thruster grids represent a major contamination source. Some of the sputtered Mo atoms can become ionised by CEX collisions with beam ions. The Mo–Xe^+ CEX cross-section is taken as $6 \times 10^{-20}\mathrm{m}^2$[19]. The neutral density of Mo is typically four orders of magnitude less than the neutral propellant density. Hence, the perturbations caused by the Mo CEX ions to the electric field is minimal and can be easily neglected with respect to the field effect due to the Xe CEX ions. The average neutral efflux density of Mo at thruster exit, n_{n_c} may be estimated from[11].

$$n_{n_c} = \frac{\mathrm{d}\eta}{\mathrm{d}t} / \left(\bar{v} A_e\right) \qquad \ldots (7)$$

where the average efflux velocity of sputtered Mo atoms is based on grid wall temperature. The Mo sputtering rate is calculated from[11].

$$\frac{\mathrm{d}\eta}{\mathrm{d}t} = YJ_{ac}/e \qquad \ldots (8)$$

Recent spectroscopical measurement of the sputtering yield at Xe ion energy of 200eV is about 0·082 atoms/ion[21,22]. The acceleration grid current is taken as 0·46 mA to be the same as that obtained from the wear test results of the NSTAR thruster[23].

The electric field surrounding the spacecraft is solved from

$$-\nabla\cdot\varepsilon\nabla\Phi = e(n_i - n_e) \qquad \ldots (9)$$

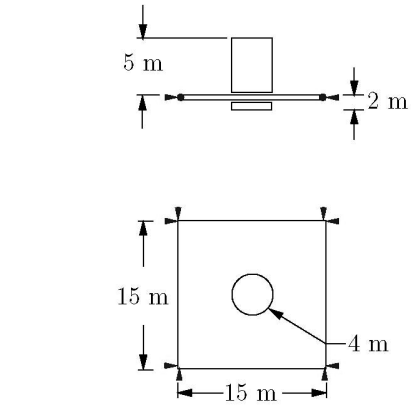
subject to the boundary condition at spacecraft surface and infinity, where the components that contribute to the total ion density are the beam ion density, the Xe CEX ion density, and the background ion density. This electric field controls the transport of CEX ions and ionised Mo, which in turn affect the space charge and the electric field. The essence of this problem is to obtain a self-consistent solution of the electric field, the space charge of the plasma, and charged particle trajectories around spacecraft.

2.2 Spacecraft model

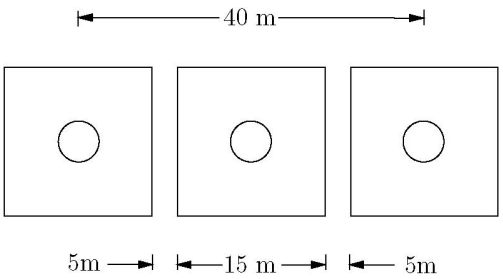
1. L2-Halo orbit formation interferometer

Our first application concerns a spacecraft formation interferometer operating in an L2-Halo orbit. The geometry and dimensions of spacecraft model as well as formation configuration are shown in

https://doi.org/10.1017/S0001924000003894 Published online by Cambridge University Press

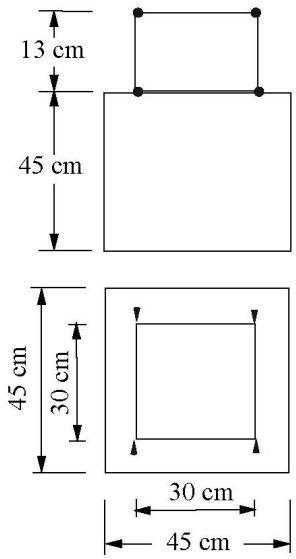


(a) Collector geometry

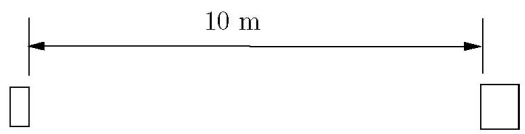


(b) In-orbit configuration

Figure 2. L2-Halo orbit interferometer formation.



(a) Spacecraft geometry



(b) In-orbit configuration.

Figure 3. LEO Micro-satellite formation.

Fig. 2. In the figure, the small arrows refer to the possible location of thrusters. We model each of the interferometer collector spacecraft as a cylinder of diameter 4m and height 5m which represents the main bus, a square thick plate of 15m side-to-side distance to represent the sun shield, a cylinder of diameter 4m and height 2m which represents an extension on the warm side of the sun shield. Each of the 16 gimbaled ion thrusters is modeled as a cylinder of 4cm diameter and 3cm height. For the formation, we assume interferometer arrangement in which all the collector spacecraft are in line with 5m separation in between.

2. Low earth orbit micro-satellite formation

Figure 3 illustrates the geometric launch configuration of the micro satellite formation and the arrangement in formation flight. In this study, we assume the follower satellite has eight miniature ion thrusters with possible locations as indicated by the small arrows. We model the leader satellite as a cube of dimensions 45 × 45 × 45cm and the follower satellite as a box of dimensions 30 × 30 × 13 cm. Each of the eight thrusters installed on the secondary satellite is modeled as a cylinder of 4cm diameter and 3cm height. In formation, the nominal separation between the two satellites is maintained at 10m.

3.0 ALGORITHM AND PARALLEL IMPLEMENTATION

A particle simulation code using the IFE-PIC algorithm is developed to solve the plume interaction problem. The IFE-PIC code solves self-consistently the particle trajectories and space charge for the CEX plasma and the electric field surrounding the spacecraft. Our emphasis here is on studying indirect impingement caused by the transport of CEX ions, hence only the CEX ions are represented by macro-particles.

The simulation is run in three phases. In the first phase, we run the IFE-PIC to generate and trace Xe CEX ions and solve for the electric field until steady-state field and trajectories are obtained. In this phase we ignore the insignificant effect of the Mo+ CEX on the electric field. Simulation particles representing CEX ions are generated at each time step according to the volumetric production rate of equation (…3). These particles, when created, are given an initial Maxwellian velocity distribution with a temperature corresponding to that of the un-ionised neutral propellant (~ 0·04 eV).

In the second phase, we freeze the electric field and rerun the IFE-PIC code to trace Mo^+ CEX ions until steady-state trajectories are obtained. In the final phase, we run the code to generate and trace Mo^+ CEX ions for further time steps to collect object-particle intersection information required for the post-processing deposition analysis.

The deposit analysis code read in the surface mesh information of the spacecraft and the data of the collected particles.

The code checks the intersection of the collected particles with the provided spacecraft surface mesh and count the number of particles passing through each triangle in the surface mesh of each entity of the spacecraft. After Mo^+ flux rates are obtained, the deposition rates can be calculated from:

$$\frac{d\xi}{dt} = 3\cdot 6\times 10^{16}\ \frac{M}{\rho}\frac{d\Gamma}{dt}\ \left[\text{A.khr}^{-1}\right] \qquad \ldots (10)$$

3.1 IFE-PIC

The basic function of an electrostatic PIC code is to solve the electric field self-consistently with the boundary conditions and the space charge of the particles from the Poisson's equation (…9) and the trajectories of each charged particle from Newton's second law

https://doi.org/10.1017/S0001924000003894 Published online by Cambridge University Press

$$\frac{\mathrm{d}}{\mathrm{d}t}(m\mathbf{v}) = \mathbf{F} = q\mathbf{E},\ \ \mathbf{v} = \frac{\mathrm{d}\mathbf{x}}{\mathrm{d}t} \quad \ldots (11)$$

The IFE-PIC is a hybrid finite-element and finite-difference particle-in-cell algorithm designed to solve the electric field accurately under complex boundary conditions while maintaining the computational speed of a standard finite-difference based PIC code[10,11]. In IFE-PIC, the Poisson's equation (…9) is solved using the immersed-finite-element (IFE) method[16,17] using a Cartesian-tetrahedral mesh. The particle-push and charge-deposit in IFE-PIC are identical to that in a finite difference based PIC using a Cartesian mesh. Unlike body-fitted, unstructured mesh-based field solvers, the IFE solver treats the internal boundary as part of the simulation domain and solves the electric field as an 'interface' problem. The mesh in the IFE method is generated independent of the interface location. If an object is present inside the simulation domain, the IFE mesh will include both interface cells, i.e. those cells that have at least one edge whose interior intersects with the interface, and non-interface cells. The details of the IFE method and IFE-PIC algorithm are discussed in Refs 10,11, and 16.

3.2 Parallel implementation

The IFE-PIC is parallelised using domain decomposition and the General Concurrent PIC (GCPIC) approach[24,25]. Each processor is assigned a subdomain with all the particles and grid points inside. When a particle moves from one subdomain to another, it is passed to the appropriate processors, which requires inter-processor communication. To ensure that the gather/scatter steps can be performed locally, each processor also stores guard cells (neighboring grid points surrounding a processor's subdomain which belong to another processor's subdomain). Inter-processor communication is necessary to exchange guard cell information. As the IFE-PIC uses a Cartesian-based tetrahedral mesh and the particles are pushed only in the Cartesian mesh, domain decomposition for IFE-PIC is the same as the standard finite difference based PIC. The message passing interface (MPI) is used for inter-processor communications.

The IFE mesh as well as the mesh-object intersections is generated locally for each sub-domain. The finite element system is constructed and stored locally on local nodes. Further details of the parallel IFE field solver can be found in Ref. 10.

The parallel implementation of PIC is based upon the UCLA Parallel PIC Framework (UPIC)[26], which provides the common components that many PIC codes share, making use of object-oriented design in FORTRAN 95. The details of the UPIC software are described in Ref. 26.

4.0 SIMULATIONS RESULTS

This section presents the results of ion thruster plume-spacecraft interaction for the two formation flight applications mentioned previously. The focus is to model the global environment of the CEX plasma surrounding an entire spacecraft in a formation flying cluster rather than detailed interactions at spacecraft surfaces. The simulations are performed using 32 processors on a Dell Xeon cluster.

4.1 Simulation setup

The simulation domain is taken to be sufficiently large to enclose the entire spacecraft formation. The cell size is taken to be sufficiently fine to resolve the estimated Debye length of the CEX plasma at spacecraft surface. The outer boundary conditions is assumed Neumann with $\partial\Phi/\partial n = 0$ on all sides of the simulation domain either because of symmetry or to impose open boundaries. The potential inside solid objects are fixed to their known values. The spacecraft bus, payloads, antennas are conductors. Hence, they are given fixed potential equal to the spacecraft uniform ground potential . Absorption particle boundary conditions are applied on all outer surfaces of the domain except on planes of symmetry where reflection boundary conditions are applied. At spacecraft surfaces, hitting ions are assumed to be adsorbed or neutralised then desorbed. Either way, particles hitting solid surfaces are taken away from the particle array.

As mentioned in Section 2, the ion beam density, neutral plume density, and electric potential at thruster exit, and electron temperature, are assumed to be the same as that observed for the NSTAR thruster on Deep Space 1. Here, we consider these parameters to have the same values as those used in Ref. 7:

$$kT_{e_0} = 1{\cdot}25\ \mathrm{eV},\ n_{b_c} = 1{\cdot}5220 \times 10^{15}\mathrm{m}^{-3},\ n_{\hat{b}_c} = 2{\cdot}3 \times 10^{17}\mathrm{m}^{-3},$$

$$dn_{cex_c}/dt = 10^{19}\mathrm{m}^{-3}.s^{-1},\ n_\infty = 7{\cdot}61 \times 10^{6}\mathrm{m}^{-3},\ \Phi_0 - \Phi_{sc} = 9\mathrm{V}$$

The PIC mesh is a uniform Cartesian mesh. The IFE mesh is a uniform Cartesian-based tetrahedral mesh with each Cartesian PIC cell divided into five tetrahedral IFE elements. The entire simulation domain is decomposed into subdomains along the axis parallel to the longer side (z-axis) using 1-D domain decomposition.

The number of simulation macro-particles was selected to be statistically large enough; typically few millions of particles. The simulation presented here typically uses ~ 10 million particles for the L2-Halo orbit mission and ~ 5 million particles for LEO orbit mission. The distribution of particle population ranges from few thousands in the cells adjacent to the thruster exit plane to few particles in the cells far away from spacecraft.

The simulation time step is calculated based on a Courant condition to assure stable calculations and minimise trajectory errors as described in Ref. 15. Since the velocity of the CEX ions increases as they move along the electrostatic field lines, the constant simulation time step should be calculated based on the maximum velocity of CEX ions. The maximum velocity of CEX ions can be estimated from the conservation of energy as

$$v_{\max} = \sqrt{2e(\Phi_0 - \Phi_{sc})/M + (v_{i_{0,\max}})^2} \quad \ldots (12)$$

where is the maximum initial velocity a CEX ion is given at birth. For the pseudo-Maxwellian distribution we use[15]. Since we are only interested in the steady state CEX plasma, the simulation can be accelerated by updating the electric field only every several PIC pushes.

The simulation results for both missions are presented and discussed below.

4.2 L2-Halo orbit interferometer mission

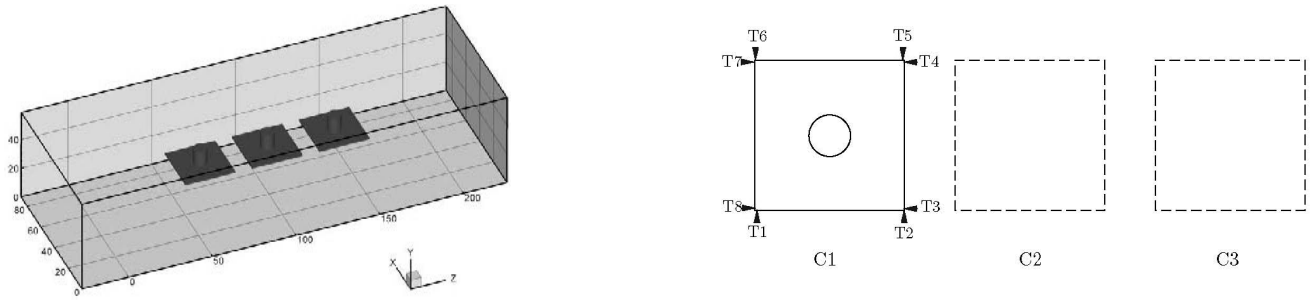
In the following, we will refer to the L2-Halo orbit interferometer formation mission as L2HALO for short. The size of the entire simulation domain is chosen as 45 × 30 × 128m and the Debye length is estimated at about 60cm. We select the cell size as 50cm. Hence, the PIC mesh will be a uniform Cartesian mesh with 90 × 60 × 256 cells as shown in Fig. 4(a).

The collector spacecraft are designated C1, C2, and C3 as shown in Figure 4 (b). The eight MiXI thrusters are designated by T1, T2, ..., T8 and are shown in the same figure only for the C1 collector. We consider six firing options (F1–F4) which are illustrated in Figure 4. So, we get four cases L2HALO/F1, ..., L2HALO/F4.

Table 1
Firing options of the L2HALO mission

Designation	Firing Thrusters		
	C1	C2	C3
F1	T1,T2	—	—
F2	T7,T8	—	—
F3	—	T1,T2	—
F4	T1,T2	T1,T2	—

https://doi.org/10.1017/S0001924000003894 Published online by Cambridge University Press



(a) Simulation domain (b) Propulsion configuration

Figure 4. Simulation domain and propulsion configuration of L2HALO.

1. CASE: HALO/F1

The steady state potential contours and trajectories of selected CEX ions are shown in Fig. 5. From the figure, we notice that the MiXI thruster plume pertains the typical winged structure of an ion thruster plume. The plume wing is evident on the outer side of T1, but nearly invisible on the inner side, at which the wings of the miniature ion thruster are overwhelmed by the huge spacecraft structure set at a negative value relative to CEX plasma. The same is true for both wings of T2 which are hardly noticeable.

The potential contours around C3 are nearly unaffected by the firing of T1 and T2 in C1. Due to the resulting plasma potential, most of the CEX ion particles are driven away from the other collectors. However, some CEX particles find their way right to C2 to hit the sun shield and even the bus. This can also be seen if we check the CEX particle flux through the spacecraft surfaces. Most CEX flux occurs on the surfaces close to the firing thrusters. It is also interesting to note that the CEX ions produced in the region between two MiXI thrusters are trapped in the potential valley between the plume cores of the two thrusters.

2. CASE: HALO/F2

Here, two T7 and T8 thrusters on C1 are firing away from the other two collectors. Steady state potential contours and trajectories of selected CEX ions are shown in Fig. 6. The potential contours in the whole domain are nearly symmetric. Most CEX ion particles flying backward go astray and do not hit any of C2 or C3 surfaces. The CEX flux is high on C1 surfaces close to firing thrusters and nearly null on C2 and C3 surfaces.

3. CASE: HALO/F3

In this case, two T1 and T2 thrusters on the middle collector C2 are firing to the side. Steady state potential contours and trajectories of selected CEX ions are shown in Fig. 7. The potential contours in the whole domain are nearly symmetric about *yz*–plane. Most CEX flux is on C2 surfaces close to firing thrusters.

But significant flux is also noticed on the inner surfaces of the sun shields of C1 and C3.

4. CASE: HALO/F4

In this case, thrusters are firing on two collectors together (T1 and T2 on both C1 and C2) as shown in Fig. 8. The CEX flux is now on the surfaces of all collectors with variable degree. Greatest flux is noticed on the inner surfaces of C1 and C2 where the firing thrusters are closest. Less flux is noticed on the outer surfaces of C1 and C2 and the inner surfaces of C3.

Maximum CEX plasma density on in the neighborhood of each of the major components of the satellites forming the L2-Halo interferometer is given in Table 2. Maximum particle deposition rates are calculated from the steady-state particle flux through satellite surfaces based on a worst-case scenario of normal impingement. The values of maximum deposition rates for all cases are given in Table 3 in units of Å/khr or Angstrom per thousand of hours. As we notice from Table 2, highest levels of CEX plasma density is noticed close to the shield of the spacecraft hosting the firing thrusters. The CEX plasma in the neighborhood of the bus and payload are much less by more than two orders of magnitude. From Table 3, we notice that maximum deposition rates in the order of one Å/khr is observed on the the shield of the spacecraft hosting the firing thrusters. On the other hand, the bus and payload of the same spacecraft experience practically negligible deposition. Other spacecraft in the formation seem well shielded from the CEX deposition.

Table 2
Maximum CEX plasma density (cm^{-3}) for L2-Halo orbit interferometer mission

	HALO/F1	HALO/F2	HALO/F3	HALO/F4
C1/Bus	6·11	6·11	7·11	10·50
C1/Payload	6·11	6·11	6·11	6·12
C1/Shield	1,194·77	1,369·80	74·43	1,255·65
C2/Bus	10·65	6·118	6·12	13·62
C2/Payload	6·11	6·118	6·11	6·11
C2/Shield	76·1	0	1,194·77	1,248·04
C3/Bus	6·11	6·11	10·73	10·65
C3/Payload	6·11	6·11	6·11	6·11
C3/Shield	0	0	76·1	80·67

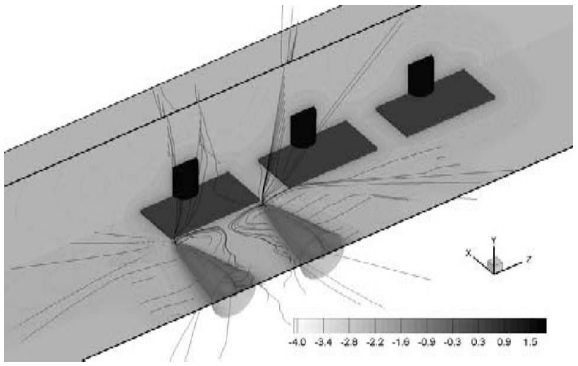
Table 3
Maximum deposition rates [Å/khr] for L2-Halo orbit interferometer mission

	HALO/F1	HALO/F2	HALO/F3	HALO/F4
C1/Bus	< 0·001	0	< 0·001	< 0·001
C1/Payload	0	0	0	0
C1/Shield	1·005	1·131	0·187	1·121
C2/Bus	< 0·001	0	< 0·001	0·014
C2/Payload	0	0	0	0
C2/Shield	0·185	0	1·005	1·170
C3/Bus	0	0	< 0·001	< 0·001
C3/Payload	0	0	0	0
C3/Shield	0	0	0·185	0·198

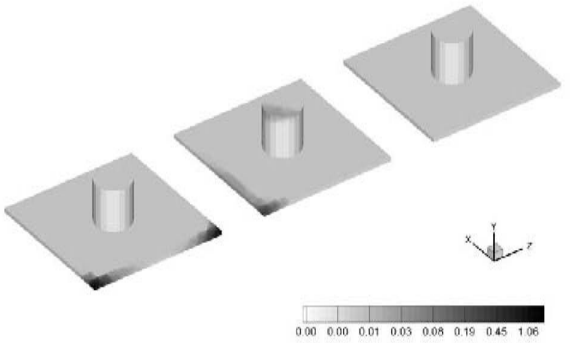
4.3 LEO Micro-satellite formation

In the following, we will refer to the LEO macro-satellite formation mission as LEO for short. The size of the entire simulation domain is chosen as 2·25 × 2·25 × 12·8m and the Debye length is estimated at about 18cm. However, we select the cell size as 5cm to better

https://doi.org/10.1017/S0001924000003894 Published online by Cambridge University Press

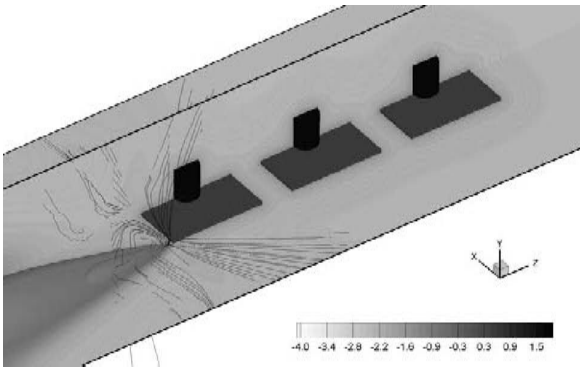


(a) XYZ-view of potential and trajectories

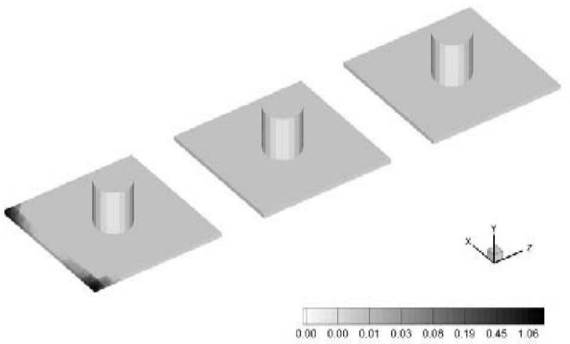


(b) CEX ion flux

Figure 5. CEX plasma of HALO/F1 (Potentials are normalised by T_{e0}).

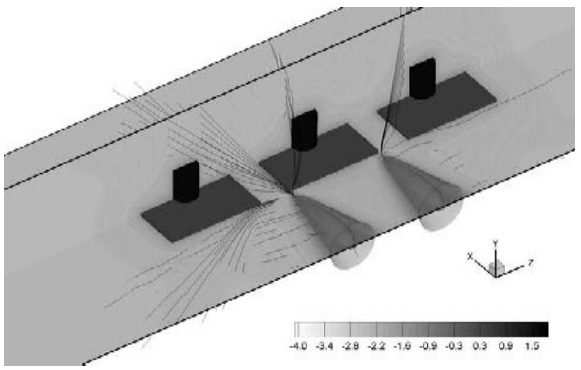


(a) XYZ-view of potential and trajectories

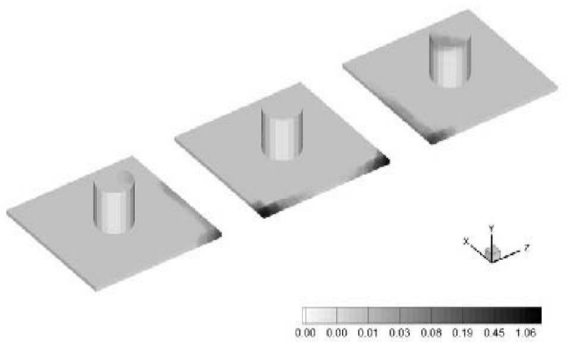


(b) CEX ion flux

Figure 6. CEX plasma of HALO/F2 (Potentials are normalised by T_{e0}).

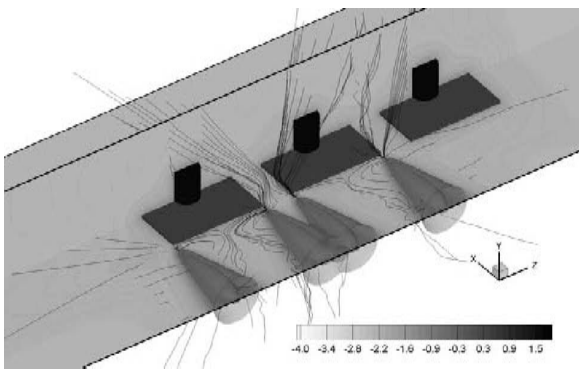


(a) XYZ-view of potential and trajectories

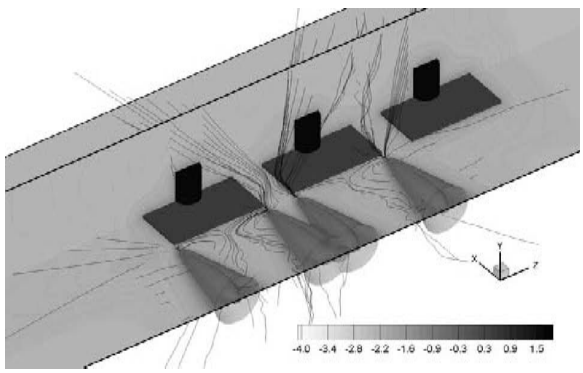


(b) CEX ion flux

Figure 7. CEX plasma of HALO/F3 (Potentials are normalised by T_{e0}).



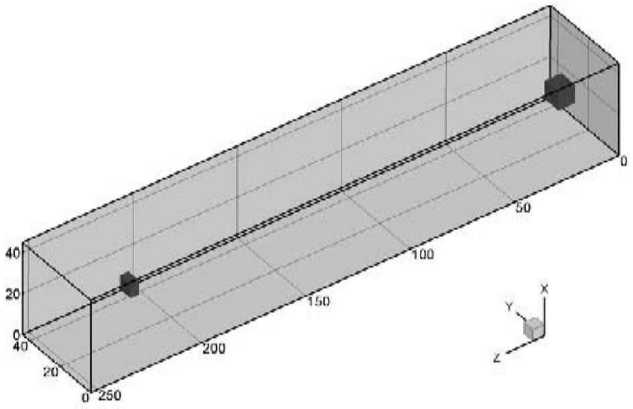
(a) XYZ-view of potential and trajectories



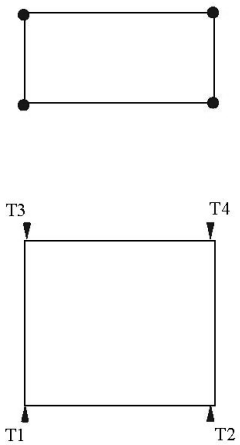
(b) CEX ion flux

Figure 8. CEX plasma of HALO/F4 (Potentials are normalised by T_{e0}).

https://doi.org/10.1017/S0001924000003894 Published online by Cambridge University Press



(a) Simulation domain



(b) Propulsion configuration

Figure 9. Simulation domain and propulsion configuration of LEO.

resolve the solution details of the spacecraft. Hence, the PIC mesh will be a uniform Cartesian mesh with 45 × 45 × 256 cells as shown in Figure 9(a).

The eight MiXI thrusters are designated by T1, T2, T3, and T4 for top thrusters; and T1', T2', T3, and T4' for bottom thrusters. Only top thrusters are shown in Figure 9(b) for clarity. We consider four firing options (F1–F4) which are illustrated in Table 4. So, we get four cases LEO/F1 ... LEO/F4.

Table 4
Firing options of the LEO mission

Designation	Firing Thrusters
F1	T1,T2
F2	T1,T2,T1',T2'
F3	T1,T1',T4,T4'
F4	T1,T2,T3',T4'

1. CASE: LEO/F1

The steady state potential contours and trajectories of selected CEX ions are shown in Fig.e 10. From this figure, we notice that the MiXI thruster plume pertains the typical winged structure. The plume wing is evident on both sides of thruster which is expected for a thruster diameter comparable to the secondary satellite dimensions. CEX ions produced in the plume region flow sideward and backward. Some of these CEX ions definitely hit the hosting satellite resulting in the high flux shown in Fig. 10 (b). A few of CEX ions travel through the far distance between the follower and leader satellites (as compared to satellite dimensions) and hit the leader satellite surface. However, the number of CEX ions hitting the leader satellite surface is very small as illustrated by the extremely low flux shown in Fig. 10(d).

2. CASE: LEO/F2

In this firing option, four MiXI thrusters on one side of the follower satellite are firing. As shown in Figure 11, the plumes of the four thrusters combine together to form one big plume with greater effect than a single thruster or double thrusters. More CEX ions are produced which is noticed through the increase in the flux of CEX ions through the surfaces of the follower satellite as shown in Figure 11(b). More flux is also noticed at the primary satellite but still very low.

3. CASE: LEO/F3

Here, we are firing T1 and T4 on the top surface and T1' and T4' on the bottom surface of the follower satellite. Figure 12. illustrates the steady state potential contours and CEX trajectories. On the follower satellite, CEX flux is greater the closer to the firing thrusters. Little flux on the surfaces of the primary satellite is noticed.

4.0 CASE: LEO/F4

In this case, we are firing T1 and T2 on the top surface and T3' and T4' on the bottom surface of the follower satellite. Figure 13 illustrates the steady state potential contours and CEX trajectories.

On the follower satellite, CEX flux is greater closer to the firing thrusters. Little flux on the surfaces of the primary satellite is noticed.

Table 5 summarises the maximum CEX plasma density in the neighborhood of each of the formation satellites. Maximum particle deposition rates for the LEO micro-satellite formation mission have been calculated and listed in Table 6. We notice that maximum CEX plasma density and maximum deposition rate are nearly doubled when the number of firing thrusters is doubled. If compared to the L2Halo formation mission, the LEO micro-satellite exhibit higher densities in the neighborhood of the secondary spacecraft, even if the same number of thrusters is firing, probably due to the closer proximity of the firing thrusters on the micro-satellite. From Table 6, we notice that significant deposition rates are observed 2 – 4 Å/khr, which might need further consideration especially for long missions.

Table 5
Maximum CEX plasma density (cm^{-3}) for the follower satellite in the LEO micro-satellite formation

LEO/F1	LEO/F2	LEO/F3	LEO/F4
644·57	1455·0	1529·6	1432·2

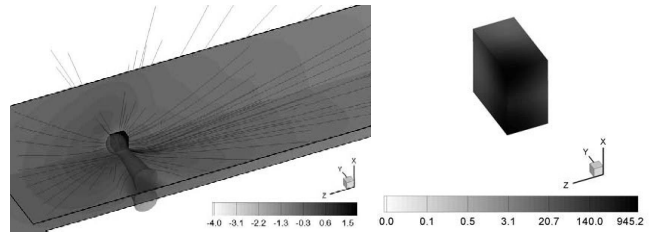
Table 6
Maximum deposition rates (Å/khr) for the follower satellite in the LEO micro-satellite formation

LEO/F1	LEO/F2	LEO/F3	LEO/F4
2·091	4·798	4·736	4·708

5.0 SUMMARY AND CONCLUSIONS

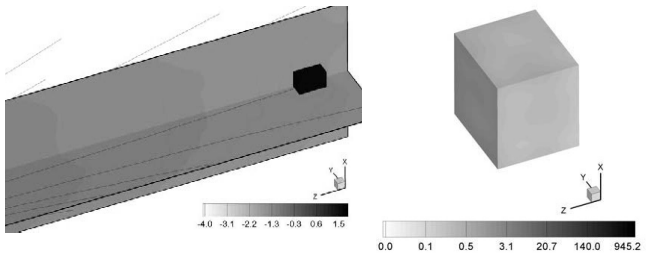
In summary, we have employed a parallel, three-dimensional electrostatic immersed-finite-element particle-in-cell (IFE-PIC) code to perform large-scale simulations of ion propulsion plume interactions for satellites in formation flight. We have considered two formation flying applications. The first is an L2-Halo orbit spacecraft formation interferometer composed of three identical collector spacecraft, to approximate the proposed ESA Darwin mission. The second mission is low Earth orbit micro-satellite formation mission similar to the MR formation satellite concept.

https://doi.org/10.1017/S0001924000003894 Published online by Cambridge University Press



(a) Potential and trajectories at secondary satellite

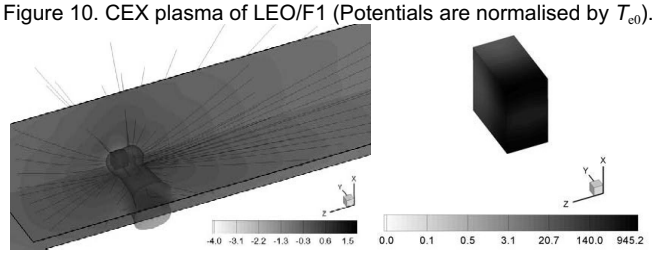
(b) CEX ion flux at follower satellite



(c) Potential and trajectories at primary satellite

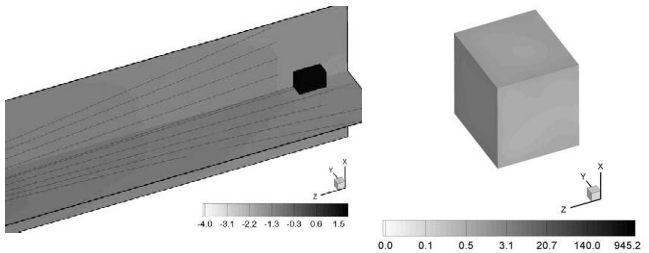
(d) CEX ion flux at follower satellite

Figure 10. CEX plasma of LEO/F1 (Potentials are normalised by T_{e0}).



(a) Potential and trajectories at follower satellite

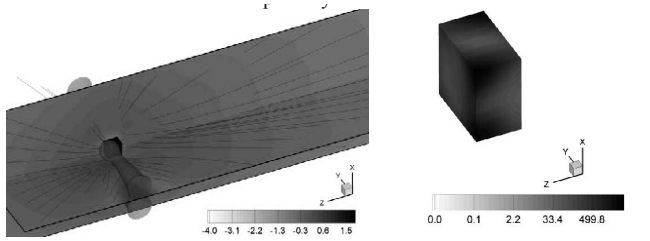
(b) CEX ion flux at follower satellite



(c) Potential and trajectories at primary satellite

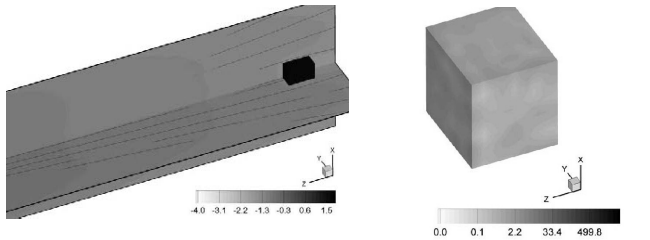
(d) CEX ion flux at primary satellite

Figure 11. CEX plasma of LEO/F2 (Potentials are normalised by T_{e0}).



(a) Potential and trajectories at follower satellite

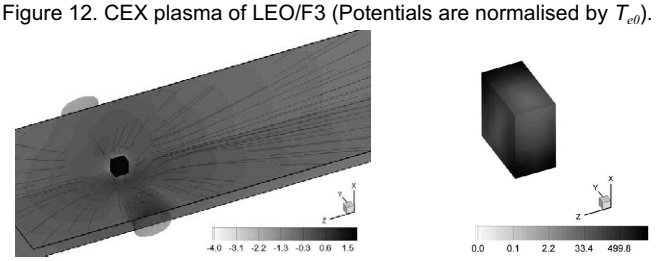
(b) CEX ion flux at follower satellite



(c) Potential and trajectories at primary satellite

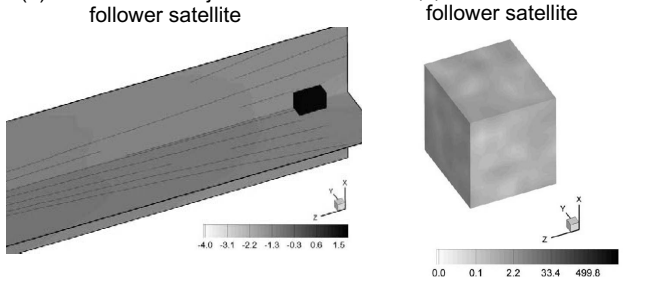
(d) CEX ion flux at primary satellite

Figure 12. CEX plasma of LEO/F3 (Potentials are normalised by T_{e0}).



(a) Potential and trajectories at follower satellite

(b) CEX ion flux at follower satellite



(c) Potential and trajectories at primary satellite

(d) CEX ion flux at primary satellite

Figure 13. CEX plasma of LEO/F4 (Potentials are normalised by T_{e0}).

For both applications, we assume that the propulsion is provided by miniature xenon ion thrusters.

The focus of this study is on indirect plume impingement on satellites outside of the direct impingement zone. Direct impingement can be easily predicted using approximate analytical plume models. Therefore, a mission designer can layout the formation configuration rationally to avoid direct impingement. Indirect impingement, on contrary, is very difficult to predict by direct rational and can only be estimated through plasma simulation or in-flight measurements.

We find that indirect plume impingement is a non-negligible factor on satellites in formation flight. For instance, for the L2Halo mission configurations considered, ion thruster firing will generate a CEX plasma environment of maximum density ranging from 6 – 100 cm^{-3} and a contamination environment of less than 1 Å/khr for the neighbouring satellites. Whereas for the micro-satellite mission configurations considered, the maximum density generated will range from 600 – 1,500cm^{-3} and the maximum contamination will range from 2 – 4·8Å/khr for the neighboring satellites. We note that these induced environments are based on the assumed thruster characteristics and operating conditions. To reduce the contamination from these levels, one would need to either use a smaller thruster and/or operate these thrusters at smaller specific impulse.

Using high-fidelity plasma simulation software makes it possible for the mission planner and spacecraft designer to avoid layouts and/or formation configurations which might compromise the eminence of critical spacecraft elements such as telescope lenses or infrared sensors.

ACKNOWLEDGMENTS

We acknowledge very helpful discussion with Dr J. Wang of Virginia Tech, USA. The plume model in this paper was based on the work previously published by him. We would like also to acknowledge discussions with Dr H. Pernick of University of Missouri-Rolla on the MR SAT mission.

https://doi.org/10.1017/S0001924000003894 Published online by Cambridge University Press

REFERENCES

1. VIGNAL, P. and PERNICK, H. Low-thrust spacecraft formation keeping, *J Spacecraft and Rockets*, 2006, **43**, (2).
2. SAMANTA ROY, R.I., HASTINGS, D.E. and GATSONIS, N.A. Ion-thruster plume modelling for backflow contamination, *J Spacecraft and Rockets*, 1996, **33**, (4).
3. VANGILDER, D.B., FONT, G.I. and BOYD, I.D. Hybrid Monte Carlo–particle-in-cell simulation of an ion thruster plume, *J Propulsion and Power*, 1999, **15**, (4).
4. WANG, J., BRINZA, D.E., YOUNG, D., NORDHOLT, J., POLK, J., HENRY M., GOLDSTEIN, R., HANLEY, J., LAWRENCE, D. and SHAPPIRIO, M. Deep Space 1 Investigations of ion propulsion plasma environment, *J Spacecraft and Rockets*, 2000, **37**, (5), pp 545-555.
5. BRINZA, D., HENRY, M., MACTUTIS, A., MCCARTY, K. RADEMACHER, J. VAN ZANDT, T., NARVAEZ, P., WANG, J., TSURUTANI, B. and KATZ, I. An overview of results from the Ion propulsion diagnostics sensors flown on DS1, AIAA 2001-0966, 39th AIAA Aerospace Sciences Meeting and Exhibit, Reno, Nevada, USA, 8-11 January, 2001.
6. BRINZA, D., WANG, J., POLK, J. and HENRY, M. Deep space 1 measurements of ion propulsion contamination, *J Spacecraft and Rockets*, 2001, **38**, (3), pp 426-432.
7. WANG, J., BRINZA, D. and YOUNG, M. Three-dimensional particle simulation modelling of ion propulsion plasma environment for deep space 1, *J Spacecraft and Rockets*, 2001, **38**, (3).
8. MANDELL, M.J., MIKELLIDES, I.G., JOHNSON, L.K. and KATZ, I. A high power ion thruster plume model, July 2004, 40th AIAA/ASME/SAE/ASEE Joint Propulsion Conference and Exhibit, Fort Lauderdale, Florida, USA, AIAA 2004–3816.
9. CELIK, M. and MARTINEZ-SANCHEZ, M. Numerical simulation of the electric thruster plume environment around the TPF spacecraft, July 2005, 41st AIAA/ASME/SAE/ASEE Joint Propulsion Conference and Exhibit, Tucson, Arizona, USA, AIAA 2005-404.
10. WANG, J., CAO, Y., KAFAFY, R., PIERRU, J. and DECYK, V.K. Simulations of Ion thruster plume spacecraft interactions on parallel supercomputer, trans. plasma science, 2006, **34**, pp 2148–2158.
11. KAFAFY, R. and WANG, J. A Hybrid grid immersed finite element particle-in-cell algorithm for modelling spacecraft-plasma interactions, *Trans Plasma Science*, 2006, **34**, (5).
12. DOOLEY, J.A. and LAWSON, P.R. Technology plan for the terrestrial planet finder interferometer, June 2005, Technical report, Jet Propulsion Laboratory, California Institute of Technology, Pasadena, California, USA.
13. WILSON, A. and MARSDEN, R. ESA's Report to the 35th COSPAR Meeting, July 2006, Technical report, Beijing, China.
14. European Space Agency, DARWIN, http://www.esa.int/science/ darwin, retrieved 12 January 2010.
15. BIRDSALL, C.K. and LANGDON, A.B. *Plasma Physics via Computer Simulation*, 1991, *Series in Plasma Physics*, The Institute of Physics.
16. KAFAFY, R., LIN, T., LIN, Y. and WANG, J. Three dimensional immersed finite element methods For electric field simulation In composite materials, *Int J Numerical Methods Engineering*, 2005, **64**, pp 940–972.
17. KAFAFY, R. Immersed Finite Element Particle-In-Cell Simulations of ion Propulsion, September 2005, PhD Dissertation, Virginia Polytechnic Institute and State University.
18. RAPP, D. and FRANCIS, W.E. Charge exchange between gaseous ions and atoms, *J Chemical Physics*, **37**, 1962, pp 2631-2645.
19. RUTHERFORD, J.A. and VROOM, D.A. Charge transfer cross sections for Hg+, Xe+, and Cs+ in collision with various metals and carbon, *J Chemical Physics*, 1981, **74**, pp 434-441.
20. WANG, J. POLK, J. BROPHY, J. and KATZ, I. Three-dimensional particle simulations of ion thruster optics plasma flow and grid erosion, *J Propulsion and Power*, 2003, **19**, (6), pp 1192-1199.
21. DOERNER, R.P., WHYTE, D.G. and GOEBEL, D.M. Sputtering yield measurements during low energy xenon plasma bombardment, *J Applied Physics*, 2003, **93**, pp 5816-5823.
22. DOERNER, R.P. and GOEBEL, D.M. Sputtering yields of ion thruster grid and cathode materials during very low energy xenon plasma bombardment, July 2003, 39th AIAA/ASME/SAE/ASEE Joint Propulsion Conference and Exhibit, Huntsville, Alabama, USA, AIAA 2003-4561.
23. POLK, J., BROPHY, J.A.J., RAWLIN, V., PATTERSON, M., SOVEY, J. and HAMLEY, J. An overview of the results from an 8200 hour wear test of the NSTAR ion thruster, June 1999, 35th AIAA/ASME/SAE/ASEE Joint Conference and Exhibit, Los Angeles, California, USA, AIAA 1999-2446.
24. LIEWER, P. and DECYK, V. A general concurrent algorithm for plasma particle-in-cell simulation codes, *J Computational Physics*, 1989, **85**, pp 302-322.
25. J. WANG and DECYK, V. 3D Electromagnetic plasma particle simulations on a MIMD parallel computer, *Computer Physics Communications*, 1995, **87**, pp 35-53.
26. DECYK, V. and NORTON, C. The UCLA parallel PIC framework, *Computer Physics Communications*, 2004, **164**, pp 80-85.

https://doi.org/10.1017/S0001924000003894 Published online by Cambridge University Press